



A Phase Separation Inlet for Droplets, Ice Residuals, and Interstitial Aerosols

Libby Koolik^{1,2,3}, Michael Roesch^{1,4}, Lesly J. Franco Deloya¹, Chuanyang Shen^{1,5}, A. Gannet Hallar^{6,7},
Ian B. McCubbin⁷, Daniel J. Cziczo^{1,2,8}

1 Department of Earth, Atmospheric and Planetary Sciences, Massachusetts Institute of Technology, Cambridge, MA 02139, USA

2 Department of Civil Environmental Engineering, Massachusetts Institute of Technology, Cambridge, MA 02139, USA

3 Ramboll, San Francisco, CA 94111, USA

4 Department of Environmental Systems Science, Swiss Federal Institute of Technology, ETH Zurich, Zurich, 8092, Switzerland

5 Department of Atmospheric and Oceanic Sciences, Peking University, 100871, Beijing, China

6 Department of Atmospheric Sciences, University of Utah, Salt Lake City, UT 84112

7 Storm Peak Laboratory, Desert Research Institute, Steamboat Springs, CO 80488

8 Department of Earth, Atmospheric and Planetary Sciences, Purdue University, West Lafayette, IN 47907 USA

5

10

15 *Correspondence to:* Daniel Cziczo (djciczo@purdue.edu)

Abstract. A new inlet for studying the aerosols and hydrometeor residuals that compose mixed-phase clouds – the phase Separation Inlet for Droplets, Ice Residuals and Interstitial aerosols (SPIDER) – is described here. SPIDER combines an omnidirectional inlet, a Large-Pumped Counterflow Virtual Impactor (L-PCVI), a flow tube evaporation chamber, and a Pumped Counterflow Virtual Impactor (PCVI) to separate droplets, ice crystals, and interstitial aerosols for simultaneous sampling. Laboratory verification tests of each individual component and the composite SPIDER system were conducted. SPIDER was deployed to Storm Peak Laboratory (SPL), a mountain-top research facility at 3210m a.s.l. in the Rocky Mountains, for a three-week field campaign. SPIDER performance as a field instrument is presented with data that demonstrates its capability of separating distinct cloud elements and interstitial aerosol. Possible design improvements of SPIDER are also suggested.

25

30



1 Introduction

A mixed-phase cloud has both liquid and ice phases present (Korolev et al., 2003; Shupe et al., 2006). For this category of clouds, the number density and mass ratio of liquid to solid water can vary. Mixed-phase clouds are important factors in aviation and climate (Shupe et al., 2008). In aviation, their supercooled droplets can cause aircraft icing and engine power loss (Strapp et al., 2016). In climate, the role clouds play in the earth's radiative budget remains uncertain (Boucher et al., 2013). As aerosol concentration increases in the atmosphere, liquid clouds may have decreased droplet size and increased spatial and temporal extent (Boucher et al., 2013). This will change the radiative forcing at the top of the atmosphere (cloud albedo effect) as well as the lifetime of a cloud (lifetime effect) (Lohmann and Hoose, 2009; Storelvmo et al., 2008). Mixed-phase clouds are particularly complicated because the partitioning of phases is critical in assessing these effects (Atkinson et al., 2013; Hirst et al., 2001; Korolev et al., 2003; Shupe et al., 2006). At present, these effects are difficult to parameterize in models due to a lack of observational research on formation, properties, and phase partitioning (Kamphus et al., 2010; Shupe et al., 2006). This has resulted in a global effort to study these clouds (Abel et al., 2014; Davis et al., 2007a; Hiranuma et al., 2016a; Kupiszewski et al., 2015; Mertes et al., 2007; Patade et al., 2015).

The microphysical formation processes of water and ice clouds are generally understood. Droplets form when a critical saturation, described theoretically by the Köhler equation, is exceeded. At this point aqueous droplets are the favored state and the particles which activate are termed cloud condensation nuclei (CCN) (Lohmann and Hoose, 2009; Wang et al., 2012). Ice nucleation is more complex. Ice can form homogeneously, via spontaneous nucleation of ice in a solution droplet, at temperatures below -40°C (Atkinson et al., 2013; Kamphus et al., 2010; Korolev et al., 2003; Storelvmo et al., 2008; Verheggen et al., 2007; Wang et al., 2012). At higher temperatures, ice forms heterogeneously through different pathways promoted by ice nucleating particles (INPs) (Atkinson et al., 2013; Kamphus et al., 2010; Lohmann and Hoose, 2009; Storelvmo et al., 2008; Tsushima et al., 2006; Verheggen et al., 2007; Wang et al., 2012). The specific properties that determine an effective INP remain poorly understood (Shupe et al., 2008).

There is also uncertainty regarding the existence of both liquid and solid water in the same environment. The accepted theory is the Wegener-Bergeron-Findeisen (WBF) process, whereby ice crystals, depending on the specific environmental temperature and humidity, grow at the expense of droplet evaporation due to thermodynamic instability (Korolev, 2007; Pruppacher and Klett, 1997). Ice crystals have a lower saturation vapor pressure than water droplets below 0°C , so the presence of crystals will lower the relative humidity and cause the droplets to shrink or, given sufficient time, evaporate completely (Shupe et al., 2006; Storelvmo et al., 2008; Tsushima et al., 2006; Verheggen et al., 2007). This effect is often limited by the concentration of ice crystals in the cloud, since ice is often less than droplet number in mixed phase clouds (Verheggen et al., 2007).

In-situ observations are required to understand the natural efficiency of INP and microphysics of mixed-phase clouds. Many experiments have occurred in the Arctic due to a prevalence of mixed-phase stratiform clouds (e.g. 41% of the time in the study of Shupe et al. (2006)) and motivated by climate change in this region, estimated to be warming approximately twice as



fast as the global average (Verlinde et al., 2007). Another research location has been the Jungfrauoch, a site in Switzerland,
65 which has high cloud coverage (37% of the time) and a prevalence of mixed-phase clouds (Kamphus et al., 2010; Verheggen
et al., 2007).

Two of the fundamental questions surrounding mixed-phase cloud formation are: (1) what is the ratio of ice to water in a cloud
and (2) what are the aerosols that act as the CCN or INPs? Currently, there are a variety of instruments that can estimate ice
or water content of a cloud. Three examples of probes that effectively measure ice or water content of a cloud are the Nevzorov
70 Probe (Abel et al., 2014; Davis et al., 2007a; Korolev et al., 1998), the Isokinetic Total Water Content Evaporator (Strapp et
al., 2016), and the Closed-Path Tunable Diode Laser Hygrometer (Davis et al., 2007b). However, these instruments do not
report information about the underlying INPs or CCN.

One technique capable of capturing ice and droplet residuals is the Counterflow Virtual Impactor (CVI) and its laboratory
counterpart, the Pumped-Counterflow Virtual Impactor (PCVI). These methods use the idea that activated droplets or ice
75 crystals are significantly larger than unactivated aerosol (Slowik et al., 2011). By separating based on mass, researchers can
study differences between activated and interstitial aerosol. This technique has been used in a large number of studies since
the mid-1980s when it was first described by Ogren et al. (1985).

The PCVI is a ground-based sampling method using vacuum-pumped air to form a stagnation plane based on the design CVI
(Boulter et al., 2006; Hiranuma et al., 2016b). A schematic of the PCVI used in this study is shown in Figure 1. A vacuum
80 pump is used to provide a “pump flow” (PF), while pressurized air is introduced as an “add flow” (AF) to the PCVI. At the
top of the PCVI is the “input flow” (IF) and at the bottom a “sample flow” (SF) is created (Boulter et al., 2006; Friedman et
al., 2013). The “effective counterflow” (ECF) is the difference of AF and SF and counteracts the IF to create a stagnation
plane. The 50% cut size or “D50” describes the smallest particle that is transmitted through the PCVI at 50% transmission
efficiency. To adjust the D50, the AF-to-IF ratio can be adjusted, reducing or increasing the inertial barrier to particle passage
85 (Kulkarni et al., 2011; Slowik et al., 2011).

Since the original characterizations by Boulter et al. (2006) and Kulkarni et al. (2011), the PCVI has been used in many studies
and adapted for use in several cloud-sampling inlets (Baustian et al., 2012; Friedman et al., 2013; Slowik et al., 2011). The
most recent advancement is the ability to build a PCVI using three-dimensional (3D) stereolithography (SLA) printing (Koolik,
2017). 3D printing allows rapid prototyping for complex devices (Jacobs, 1992), making the development of cheaper, more
90 efficient PCVIs possible. This development mitigates costs, decreases machining time, avoids misalignment issues, and allows
for rapid tests of various structural improvements (Koolik, 2017).

2. Instrument Theory and Design

SPIDER is a vertically-aligned inlet system with three distinct outlet channels for sampling interstitial (or ‘unactivated’) aerosols, droplet residuals, and ice crystal residuals (Figure 2). It is comprised of four components: omni-directional inlet, L-
95 PCVI, droplet evaporation chamber, and PCVI.



The omni-directional inlet prevents entry of large particulates, such as precipitation and blowing snow, into the system. It was designed using a computer-aided design (CAD) program (Solidworks 2015; Dassault Systems) and printed on a SLA printer (Form2, Formlabs Inc.). The opening slit of the inlet narrows from 4 mm down to 3 mm before the particles enter the inlet fully. Once inside the inlet, particles too large to follow the streamlines are lost due to impaction.

100 Directly downstream of the omni-directional inlet is the L-PCVI. The 3D printed L-PCVI was based on the design of the IS-PCVI described by Hiranuma et al. (2016). When operated with a 70 L min⁻¹ input flow and 7 L min⁻¹ counterflow, the IS-PCVI is capable of achieving a D50 of approximately 9 μm (Hiranuma et al., 2016). By operating the L-PCVI with an AF-to-IF flow ratio of 0.19, the D50 is ~20 μm; only activated droplets and ice crystals are large enough to exit the SF, with droplets and ice crystals at 10 μm or larger (Kleinman et al., 2012; Pruppacher and Klett, 1997; Rogers and Yau, 1989). The flow rates
105 used in SPIDER are described in Table 1.

The Weber Number, N_{We} , was calculated using the flows of the L-PCVI to ensure that large droplets and ice crystals are transmitted through the L-PCVI without breakup. N_{We} describes the ratio of the Bernoulli pressure caused by surrounding and opposing flow on a falling droplet to the surface tension of the droplet (Pruppacher and Klett, 1997). Droplet disruption has been estimated to occur for N_{We} significantly larger than 10 (Pruppacher and Klett, 1997). The following expression was used
110 to solve for N_{We} and maximum droplet diameter (d_{max}):

$$N_{We} = \frac{\rho_a d_{max} U_\infty^2}{\sigma} \quad (1)$$

$$d_{max} = \frac{8\sigma}{C_D \rho_a U_\infty^2} \quad (2)$$

where ρ_a refers to density of the surrounding air, σ is the surface tension of the droplet, U_∞ is the difference between the droplet velocity and the gas velocity, and C_D refers to the drag coefficient (Pekour and Cziczko, 2011). The droplet velocity was
115 approximated using the following expression from Pekour and Cziczko (2011):

$$\frac{m_p v_i^2}{2} = \frac{m_p v_{i-1}^2}{2} + \Delta x \cdot F_{D_{i-1}} \quad (3)$$

$$F_D = \frac{\pi C_D \rho_a v^2 \chi^2 d_{max}^2}{8 C_c} \quad (4)$$

where C_D refers to the drag coefficient, χ is the shape factor, and C_c is the slip factor.

N_{We} as a function of distance along the L-PCVI was modeled for droplets varying in size from 1 to 75 μm using SPIDER's L-
120 PCVI IF of 42 SL min⁻¹ (Figure 3). The maximum N_{We} calculated was approximately 0.3, signifying that droplets are not expected to break up in the L-PCVI using SPIDER's flow rates.

Ice crystals and supercooled droplets that pass through the L-PCVI enter the droplet evaporation chamber, which utilizes the WBF process. The chamber is held at -16° C because the difference in saturation vapor pressure between water and ice is at maximum. By the end of the chamber, the ice crystals and water droplets exist in two separate size modes (i.e., ice crystals
125 maintain their size while droplets evaporate).

Below the droplet evaporation chamber a PCVI is mounted. For this work both a machined (Model 8100, BMI Inc.), described by Boulter et al. (2006) and Kulkarni et al. (2011), and a 3D printed PCVI, described by Koolik (2017), were used and exhibited



the same performance. In the SPIDER setup, the PCVI is operated with a D50 of $\sim 2 \mu\text{m}$, so ice crystals will be entrained into the SF of the PCVI while the evaporated droplet residuals will be removed through the PF. These flows used are summarized in Table 1.

N_{wc} was calculated for the PCVI and found to be higher for all droplets than in the L-PCVI due to higher gas velocity (Figure 4). Still, the maximum N_{wc} for the largest droplet remained below the threshold of 10, signifying that remaining droplets should not break up before rejection. Note that the 3D printed PCVI (Figure 1) incorporates the Kulkarni et al. (2011) slanted instead of stepped inlet nozzle.

Using this methodology, SPIDER offers the ability for simultaneous sampling of interstitial aerosol, droplet residuals, and ice crystal residuals through the three outlet channels – the PF of the L-PCVI, PF of the PCVI, and the SF of the PCVI, respectively. These can be connected to chemical composition analyzers or optical particle counters for further analysis.

3. Methodology

3.1. 3D Component Fabrication

SPIDER incorporates a number of parts that were 3D printed. SLA printing involves the photopolymerization of a liquid resin by a laser in a layer-by-layer process. This mechanism was chosen due to its high resolution, high surface quality, low shrinkage, and low distortion in printed parts (Bartolo, 2011; Bhushan and Caspers, 2017; Hagiwara, 2004). There are drawbacks and common errors that occur with SLA, including overcuring (solidified material fails to bind with the layer below it) and time-intensive post-processing (Jacobs, 1992; Wong and Hernandez, 2012). The printer (Form 2, Formlabs Inc.) used for the SPIDER components uses a 405 nm UV laser to cure specific coordinates in a resin bath to create the part in a layered structure (Formlabs, 2015). Parts for SPIDER were printed using a ‘tough resin’ (FLTOTL03, Formlabs Inc.) with a 100- μm layer resolution.

The following procedure was utilized for creating 3D printed parts: A part was virtually designed using Solidworks. The Solidworks assembly tool was used to verify that multiple parts would fit together as designed. Then the part was exported as a stereolithography file (.STL) and uploaded to a 3D printing software (Preform, Formlabs Inc.) where the part was oriented and support structures were added, either automatically by the program or manually by the user. The contact points attached to the part are small (0.5 mm) for easy removal after printing. From Preform, the part is uploaded onto the printer. After prints were completed, the parts were post-processed following the same procedure as described by Roesch et al. (2017): first, they are shaken in a bath of isopropyl alcohol (IPA) and then left for approximately 20 minutes to remove uncured resin. Second, the parts are exposed to UV light inside a curing box with the same wavelength as the printer’s laser. Third, the support structures were removed and the surface wet-sanded.



3.2. Operation Procedure

The SPIDER startup routine was designed to ensure no flow blockage moving from the bottom-upwards. The first step is to connect the critical communication lines from SPIDER to the computer via USB cables; these include an Arduino, which transmits data from the temperature sensors (Figure 2); an Alicat-BB9, which controls and reports the flow values through each mass flow controller (MFC); and the aerosol and residual measurement devices, most typically optical particle counters on the aerosol and droplet residual stages and an optical particle sizer on the ice residual stage. Second, the vacuum pump and pressurized air were turned on to provide flows to the MFCs. Next, the PCVI flows were turned on by setting the AF followed by the PF. This started the flow through the chamber. The last step was to turn on the flows for the L-PCVI, again turning on AF before PF. At each point in this process, the operator verified via pressure measurements or achieved flow rates that no flow problems had occurred. Finally, the user turned on the low-temperature cooling bath (Proline RP 1290, Lauda-Koenigshofen) and flushed the chamber with dry, filtered air.

4. Verification Experiments

4.1. L-PCVI

Hiranuma et al. (2016) described the expected working conditions of the L-PCVI at different flow ratios. The operating ratio of AF to IF in L min^{-1} in laboratory conditions in SPIDER is approximately 0.19, so the D50 of the L-PCVI is expected to be 20-30 μm . The optical particle counter (OPC, OPC-N2, Alphasense) and the optical particle sizer (OPS, Model 3330, TSI), detect particles up to 17 and 10 μm , respectively, so a characterization of the L-PCVI in the style of Boulter et al. (2006) characterization of the PCVI was not possible. Instead, measurements over a range of expected D50 was used to show that the L-PCVI rejects particles as described in Hiranuma et al. (2016).

To find the lower bound of the D50 using SPIDER's flows, 10 μm polystyrene latex (PSL) spheres were generated using a 1.7 SL min^{-1} flow into the PROTeGE wet particle generation system (Roesch et al., 2018). Particles were first introduced into the L-PCVI having the PF and AF off to provide information about the aerosol size distribution generated by PROTeGE. After sampling to determine the average size distribution, the flows on the L-PCVI were turned on. The L-PCVI was run with the flows described in Table 1: the PF was 42.5 SL min^{-1} and the AF was 10.0 SL min^{-1} . In the configuration with the L-PCVI flows off, it is expected that there would be no particles in the PF but particles in the SF. When the L-PCVI flows are on, the opposite is expected. Samples were taken at a 1-second resolution in both the PF and SF of the L-PCVI. One OPC was connected to the PF of the L-PCVI; the OPS was connected to the SF of the L-PCVI.

Figure 5A and 5B show the average number concentration obtained in the PF and SF, respectively. The L-PCVI flows are initially off, and particles are only measured in the SF and not in the PF. The AF is turned on approximately 1900 seconds into the measurement and the PF 100 seconds later. When the L-PCVI flows are off, the SF has a concentration of 10 μm particles;



when the L-PCVI flows are on, these particles appear in the PF. When only the AF is on particles are rejected through the IF, resulting in no detectable signals in the PF or SF. From this, the cut size of the L-PCVI is larger than 10 μm .

The second experiment replicated measurements performed by Hiranuma et al. (2016) using an IF of 50 L min^{-1} and an AF of 7 L min^{-1} to achieve an AF-to-IF ratio of 0.14. With these flows, Hiranuma et al. (2016) report a D50 of 22 μm . To create particles larger than this expected D50, droplets were generated using a commercial droplet generator (“DG”, MD-K-130, Microdrop Technologies) with a 30 μm nozzle. The droplet size leaving the nozzle was observed to be ~ 50 μm in diameter using a high resolution magnification camera and image analysis software. A calculation of evaporation using system relative humidity and distance to the inlet of the L-PCVI suggests that the droplets entering the L-PCVI were ~ 40 μm . Droplets were created from an ammonium sulfate (AS) solution of 5 g L^{-1} . The residuals size of these droplets was calculated to be approximately 3.7 μm .

First, a measurement of droplet transmission and residual size was performed. The DG was placed 5 mm above the L-PCVI. A stream of droplets was introduced through the L-PCVI without PF or AF on (Figure 6A). The OPS was connected to the L-PCVI with a flow splitter, such that 1 L min^{-1} entered the OPS and 1 L min^{-1} as bypass flow through a MFC. The results of this measurement indicate that the residual size after residence time in the apparatus is approximately 4.7 μm . This is slightly higher than the dry residual size of the salt solution, consistent with incomplete efflorescence at the system humidity.

Next, the L-PCVI flows were turned on and measurements of the resulting particles in the SF conducted (Figure 6B). Again, a peak of particles in the 4.7 μm size bin was observed, suggesting that the droplets are transmitting and then evaporating, leaving the incompletely effloresced particles. To complete this test, the PF of the L-PCVI was terminated and only the AF was left on (Figure 6C). Here, essentially no particles are transmitted through the L-PCVI. We conclude that the particles collected in Figure 6B are the result of droplets large enough to pass through the stagnation plane. Together, these two experiments provide sufficient information to approximate the D50 of the L-PCVI in the range predicted by Hiranuma et al. (2016) using their flow ratio and values and that the 3D printed L-PCVI works. Figure 7 shows the expected result superimposed onto a figure from Hiranuma et al. (2016). Further experimentation on the 3D printed L-PCVI should be done to resolve the D50.

4.2. Droplet Evaporation Chamber

4.2.1. Droplet Evaporation

In order to demonstrate that droplets are able to evaporate in the chamber, a model of droplet evaporation was considered based on the equation of evaporation described by Lohmann et al (2016):

$$r(t) = \sqrt{r_0^2 + 2 \left(\frac{S-1}{F_k + F_d} \right) t} \quad (5)$$

where r_0 is the initial droplet radius and S is the supersaturation. F_k and F_d are defined as:

$$F_k = \rho_w \left(\frac{L_v^2}{K R_v T^2} \right) \quad (6)$$

$$F_d = \rho_w \left(\frac{R_v T}{D_v e_{s,w}(T)} \right) \quad (7)$$

where ρ_w is the density of liquid water, L_v is the latent heat of vaporization, D_v is the diffusion coefficient for water vapor in
220 air, $e_{s,w}$ is the saturation vapor pressure of water, and K is the coefficient of thermal conductivity in air. This equation is
considered valid for large droplets, as it neglects the effects of solution and curvature of the droplet. When sampling from
clouds, the droplets should satisfy this assumption.

The model was run with the approximate chamber dimensions for a variety of initial droplet sizes (5-50 μm) at different system
225 saturations (0.25, 0.5, 0.75, and 1) (Figure 8). In the simulation where $S = 1$, all of the droplets retain their original size. In the
other three simulations, the 5 and 12.5 μm droplets fully evaporate by the end of the chamber. The 25 μm droplet evaporates
fully when supersaturation is equal to or lower than 0.5.

From these models, it is expected that droplets equal to or smaller than 12.5 μm in diameter will fully evaporate before reaching
the PCVI below supersaturations of ~ 0.9 . Droplets between 12.5 and 25 μm in diameter will evaporate if the chamber
230 supersaturation is below 0.5. Given that the 12.5 μm droplets evaporate halfway through the chamber when supersaturation
was 0.75, it is likely that the smaller droplets in the range of 25-50 μm evaporate at supersaturations between 0.5-0.75 as well.
Droplets larger than 25 μm will likely not evaporate fully within the chamber at any supersaturation; this sets an upper limit
to the SPIDER capability.

In practice, the relative humidity (RH) of the L-PCVI AF and in the chamber determine the saturation droplets experience and
235 evaporate into. A static SPIDER at -16°C with ice coated walls has a relative humidity with respect to ice that is, by definition
saturation, but $\sim 85\%$ RH with respect to liquid water which is validated by hygrometer measurements. In practice the dry L-
PCVI sample flow will reduce this to $\sim 75\%$ RH. In this condition a maximum hydrometeor (droplet) size in the $\sim 20\ \mu\text{m}$ can
be fully evaporated in the chamber. A combination of lower RH (i.e., dry flow tube walls) and reduced droplet size but
incomplete evaporation can extend the upper droplet size to $\sim 25\ \mu\text{m}$.

4.2.2. Sustaining Ice Crystals

240 To verify that ice crystals are maintained throughout the chamber, an experiment was performed using the DG. Droplets of
approximately 40 μm in diameter generated from a $0.6\ \text{g L}^{-1}$ AS solution were introduced into the chamber close to the entry
point of fluid from the chiller. The chiller was set to -65°C , below the homogeneous freezing threshold of $\sim -38^\circ\text{C}$ (Koop et
al., 2000). Because the droplets are immediately exposed to this temperature, it is expected that the droplets would rapidly.
The ice crystals pass down the chamber until the PCVI, which was run with flows to achieve a D50 of 2.7-3.8 μm (Figure 9).
245 The resulting particle concentration in the PCVI SF, which is the ice crystal residual flow, is consistent with the initial
concentration of particles being frozen. A calculation of the residual size of AS expected yields $\sim 1.4\ \mu\text{m}$, so it appears that the
ice crystals are passing through the stagnation plane of the PCVI but not sublimating or evaporating fully by the time they
reach the OPS.



4.3. PCVI

250 A validation of the 3D Printed PCVI is performed in Koolik (2017). Experiments were performed following Boulter et al. (2006) and Kulkarni et al. (2011). A polydisperse particle flow was used and the OPS was connected to the SF of the PCVI. Measurements at 1-second resolution were made while the PCVI flows were off to capture the distribution of particles in the input flow (Figure 10A). Next, the PCVI flows were turned on (PF set to 7.7 SL min^{-1} and AF set to 2.0 SL min^{-1}) and measurement were repeated (Figure 10B). Finally, the OPS was disconnected from the SF and reconnected to the PF (i.e., the rejected particles, Figure 10C). A comparison of Figures 10A and 10C was performed to show the PCVI was functioning correctly. In a functional PCVI, the small particles should be rejected (and pumped away in the PF), so there should be a comparable number of particles in the small bins of the SF when the PCVI flows are off to the number of particles in the small bins of the PF when the PCVI flows are on. The concentrations of particles in the three smallest bins from the operational PCVI's PF are within 15% of those recorded when the PCVI flows were off and the OPS was attached in the SF region. As
255 rejected particles, Figure 10C). A comparison of Figures 10A and 10C was performed to show the PCVI was functioning correctly. In a functional PCVI, the small particles should be rejected (and pumped away in the PF), so there should be a comparable number of particles in the small bins of the SF when the PCVI flows are off to the number of particles in the small bins of the PF when the PCVI flows are on. The concentrations of particles in the three smallest bins from the operational PCVI's PF are within 15% of those recorded when the PCVI flows were off and the OPS was attached in the SF region. As
260 the particle diameter approaches the expected D50, the concentrations increase to within 50% of each other. It is expected that the concentrations of particles in the PF larger than the theoretical D50 will be significantly smaller than their counterparts in the SF sample because these larger particles are transmitting through the SF of the PCVI with flows on and not being pumped away in the PF.

A D50 was calculated for the PCVI of $5.2 \mu\text{m}$ from the measurements of ambient air rejection. To calculate the D50, average
265 concentrations for each size bin were calculated for both the samples with the PCVI flows on and with the PCVI flows off. From each of these, the transmission efficiency of each bin size was calculated by dividing the ratio of particles transmitted with PCVI flows on over those with PCVI flows off. The data were fitted with a sigmoidal fit and the D50 was the particle diameter size that corresponded to 50% of the maximum transmission efficiency on the sigmoid. An example of the resulting curve and sigmoidal fit is shown in Figure 11. The operational flows used for SPIDER are summarized in Table 2.

270

5. Storm Peak Laboratory Field Campaign

5.1 Storm Peak Laboratory Field Site

The Desert Research Institute's Storm Peak Laboratory (SPL) is located near Steamboat Springs in north-western Colorado at 40.45°N , 106.74°W , 3210 m above sea level (Borys and Wetzel, 1997). SPL is located on the western side of the Rocky
275 Mountains in the United States (Borys and Wetzel, 1997). This exposes SPL to prevailing westerly flow that allows for orographic lifting and cloud formation (Borys and Wetzel, 1997). During the winter, SPL is often enshrouded in clouds that contain supercooled liquid and ice crystals, making it an ideal site for sampling cloud condensation nuclei (CCN) and ice nucleating particles (INP) (Friedman et al., 2013; DeMott et al., 2010). In addition, long-term measurements made at SPL have allowed studies of the decadal trends in background aerosol properties (Asmi et al., 2013). These aerosol studies supplement
280 simultaneous measurements of supercooled liquid cloud droplet and ice particle size (e.g., Lowenthal et al., 2019). SPL is a



measurement suite for aerosol and cloud properties, coupled with meteorological instruments that can provide additional information about ambient environmental conditions and supplement the data collected by SPIDER. This made SPL an ideal site for deploying SPIDER to test its efficacy for sampling clouds.

5.2 Field Measurements

285 SPIDER was deployed at SPL for three weeks during January 2019 and sampled from the 20th-21st and the 23rd to test how well it measures in background, non-cloudy conditions and during cloudy conditions to better understand cloud microphysical processes. SPIDER was setup indoors and connected to an inlet that collected ambient air and cloud elements. The OPC attached to SPIDER was used to measure cloud droplet residuals and the Droplet Measurement Technologies Single Particle Soot Photometer Extended Range (SP2-XR) was used to measure ice crystal residuals. The SP2-XR allowed for higher
290 sampling frequency and higher sizing resolution (100 nm - 540 nm) for the ice crystal residuals. Temperature ranged from -5 to -20 °C and wind speed ranged from 0-10 m/s during the entire study period (Figure 12). Background aerosol conditions were typically low, with occasional large spikes in particle concentrations (Figure 13). During the four-day study period, there were two clear periods and three mixed-phase cloudy periods when SPIDER was tested. There was visual verification when SPIDER was in a clear or cloudy period in addition to data from the cloud imaging probe data at SPL (Figure 14, top row).

295 One of the primary concerns was that suspended snow would blow into the inlet, influencing ice crystal residual counts for SPIDER. Our data showed there was little to no association between wind speed and ice crystal concentrations during clear periods (Figure 15). However, there were background ice crystal residual concentrations detected by the ice crystal channel despite clear conditions (Figure 16, period 2). This suggests that there was some background windblown snow entering the inlet prior to entering the cloudy period (Figure 16, period 3). The average wind speed during clear periods was 2.2 m/s (max:
300 5.5 m/s) for period 1 and 6 m/s (max: 8.3 m/s) for period 2. Wind speeds ranging between 4-11 m/s are required for fresh snow transport (Li and Pomeroy, 1997). This would help explain why there were some ice crystal residuals being detected during the first and second study period (Figure 14, bottom row, January 20th and January 21st from 14:00-15:30). Although, the enhancement factor from the PCVI also contributes to the ice residual concentrations seen on clear days (Slowik et al., 2011). Blowing snow was minor in our study and was not associated with higher ice crystal residual concentrations. This is similar
305 to Lowenthal et al.'s (2019) study, which suggested that the ice crystal residual concentrations observed were not influenced by blowing snow. They suggested that the interactions between orographic and synoptic dynamics are responsible for the ice crystal concentrations observed in their study and may have been the case for this study at SPL as well. However, more studies should be done during periods of higher wind speeds, as they may influence SPIDER's ice crystal residual concentration.

310 Despite background concentrations in the ice crystal residual channel, as SPIDER went into cloudy periods, there was a change in the ice crystal residual size distribution that followed similar trends to the cloud imaging probe (Figure 14). The particles that were measured by the SP2-XR ice crystal channel during the clear periods had small diameters, with most under 200 nm (Figures 17A and 17B). Figure 17A shows higher ice crystal concentrations due to increased ambient aerosol concentrations possibly generated by new particle formation (NPF) (Figure 13, period 1) (Shen et al., in prep). This corresponds with Hallar



et al.'s (2011 and 2016) observations of NPF at SPL during the mid-afternoon and why SPIDER picked up on the higher
315 ambient aerosol concentrations. There was a transition period between periods 2 and 3 (Figure 16, striped period) that went
from clear to wisps of clouds. At around 5:15 PM (MDT), SPIDER entered a cloudy period and the ambient number size
distribution changed with an increase in size from ultrafine particles in Aitken mode to fine particles in accumulation mode
where coagulation and condensation are taking place. The ice crystal channel (Figure 17C) during the cloudy period shows
higher concentrations, with an increase between 200 nm - 500 nm that is not seen during the clear periods (Figures 17A and
320 17B). This is consistent with the finding of DeMott et al. (2010) of the correlation of INPs with aerosol >500 nm diameter.
Due to the lower sizing and timing resolution of the cloud droplet residual channel, we were unable to come to meaningful
conclusions. Future studies at SPL with SPIDER should focus on higher particle sizing resolution for the cloud droplet channel
and for extended ranges beyond 500 nm for the ice crystal channel.

6. Conclusion and Future Work

325 The laboratory verification and field experiments showed that both the individual components and composite SPIDER worked
as designed. In the verification measurements, each component of SPIDER was isolated and tested to validate that it would
perform its role in the overall system. These included the L-PCVI, the droplet evaporation chamber, and the PCVI. Once each
component was verified individually, a test was done to ensure that the combination of instruments also functioned.

Future measurements should be performed to further refine the performance of both the L-PCVI and the droplet evaporation
330 chamber. A full characterization of the L-PCVI would define the flow rates for obtaining the ideal D50 to segregate droplets
and ice crystals from interstitial aerosol. Similarly, it would be beneficial to perform further laboratory experiments on droplet
evaporation.

SPIDER was deployed at SPL in Colorado, where it proved its capability as a field instrument. As part of the proof-of-principle
campaign, SPIDER demonstrated that it is robust enough to be deployed to a remote field location and is minimally influenced
335 by windblown snow. Data from mixed phase cloud events exhibited elevated counts of ice residuals compared to clear days
and the sizing of the ice residuals collected by SPIDER corroborated well with previous fieldwork studies that have looked
also looked at ice residual size distributions. Future experiments with SPIDER will include a higher time and size resolution
OPC on both the interstitial aerosol channel and cloud droplet channel to further evaluate its efficacy for simultaneous sampling
of interstitial aerosols, cloud droplets and ice residuals.

340 The goal while designing SPIDER was to develop a comprehensive inlet for sampling and segregating cloud elements. Through
the verification tests and the field campaign, it has been demonstrated that SPIDER is capable of sorting the three components
of mixed-phase clouds into distinct channels. The next step is to couple SPIDER with chemical analyzing instruments. Mass
spectrometry, for example, can be used to determine the differences between the particles that nucleate ice and those that
nucleate droplets in mixed-phase clouds. This work could have significant implications on modeling efforts, which have to



345 make assumptions about cloud nucleation capabilities of various aerosols. With sufficient data, the results can be integrated
into global climate models and used to understand the changing climate (Shupe et al. 2008).

7. Acknowledgements

We would like to thank the William and Kumi Martin Foundation and the National Science Foundation (Grants AGS-1749851
350 and AGS-1749865) for funding. L. Koolik would like to thank the MIT Department of Civil and Environmental Engineering
for providing fellowship funding. We gratefully acknowledge Eric Kelsey and the staff of the Mount Washington Observatory
for their assistance with the logistics associated an initial proof of concept study. We also thank the other members of the
Cziczo Group at MIT for their assistance throughout the development of SPIDER. The authors appreciate the dedication,
commitment, and effort of Maria Garcia and Dan Gilchrist towards the deployment of SPIDER at SPL. We further thank
355 Droplet Measurement Technology for the use of an SP2-XR for characterization of the ice residual channel. The Steamboat
Ski Resort provided logistical support and in-kind donations. The Desert Research Institute is a permittee of the Medicine-
Bow Routt National Forests and is an equal opportunity service provider and employer.

References

- Abel, S. J., Cotton, R. J., Barrett, P. A. and Vance, A. K.: A comparison of ice water content measurement techniques on the
360 FAAM BAe-146 aircraft, *Atmos. Meas. Tech.*, 7, 3007–3022, doi:10.5194/amt-7-3007-2014, 2014.
- Alicat Scientific: Technical Data for Alicat MC and MCR Mass Flow Controllers, , 30, 1–5, 2016.
- Asmi, A., Collaud Coen, M., Ogren, J. A., Andrews, E., Sheridan, P., Jefferson, A., Weingartner, E., Baltensperger, U.,
Bukowiecki, N., Lihavainen, H., Kivekäs, N., Asmi, E., Aalto, P. P., Kulmala, M., Wiedensohler, A., Birmili, W., Hamed,
A., O'Dowd, C., G Jennings, S., Weller, R., Flentje, H., Fjaeraa, A. M., Fiebig, M., Myhre, C. L., Hallar, A. G., Swietlicki,
365 E., Kristensson, A., and Laj, P. (2013), Aerosol Decadal Trends – Part 2: In-situ Aerosol Particle Number Concentrations
at GAW and ACTRIS Stations, *Atmos. Chem. Phys.*, 13, 895-916, doi:10.5194/acp-13-895-2013.
- Atkinson, J. D., Murray, B. J., Woodhouse, M. T., Whale, T. F., Baustian, K. J., Carslaw, K. S., Dobbie, S., O'Sullivan, D.
and Malkin, T. L.: The Importance of Feldspar for Ice Nucleation by Mineral Dust in Mixed-Phase Clouds, *Nature*, 498,
355–358, 2013.
- 370 Bartolo, P. J., Ed.: *Stereolithography: Materials, Processes, and Applications*, illustrate., Springer Science & Business Media.,
2011.
- Baustian, K. J., Cziczo, D. J., Wise, M. E., Pratt, K. A., Kulkarni, G., Hallar, A. G. and Tolbert, M. A.: Importance of aerosol
composition, mixing state, and morphology for heterogeneous ice nucleation: A combined field and laboratory approach,
J. Geophys. Res. Atmos., 117(6), 1–13, doi:10.1029/2011JD016784, 2012.
- 375 Bhushan, B. and Caspers, M.: An overview of additive manufacturing (3D printing) for microfabrication, *Microsyst. Technol.*,
23(4), 1117–1124, doi:10.1007/s00542-017-3342-8, 2017.



- Borys, R. D., & Wetzel, M. A. Storm Peak Laboratory: A Research, Teaching, and Service Facility for the Atmospheric Sciences. *Bulletin of the American Meteorological Society*, 7(70), 10, 1997.
- 380 Boucher, O., Randall, D., Artaxo, P., Bretherton, C., Feingold, G., Forster, P., Kerminen, V.-M., Kondo, Y., Liao, H., Lohmann, U., Rasch, P., Satheesh, S. K., Sherwood, S., Stevens, B. and Zhang, X.-Y.: Clouds and Aerosols, in *Climate Change 2013: The Physical Science Basis. Contribution of Working Group I to the Fifth Assessment Report of the Intergovernmental Panel on Climate Change*, pp. 571–657, Cambridge., 2013.
- Boulter, J. E., Cziczko, D. J., Middlebrook, A. M., Thomson, D. S. and Murphy, D. M.: Design and Performance of a Pumped Counterflow Virtual Impactor, *Aerosol Sci. Technol.*, 40(11), 969–976, doi:10.1080/02786820600840984, 2006.
- 385 Dallas Semiconductor: DS18B20 Temperature Sensor. [online] Available from: <http://datasheets.maximintegrated.com/en/ds/DS18B20.pdf>, n.d.
- Davis, S. M., Avallone, L. M., Weinstock, E. M., Twohy, C. H., Smith, J. B. and Kok, G. L.: Comparisons of in situ measurements of cirrus cloud ice water content, *J. Geophys. Res.*, 112, 1–15, 2007a.
- Davis, S. M., Hallar, A. G., Avallone, L. M. and Engblom, W.: Measurement of Total Water with a Tunable Diode Laser Hygrometer : Inlet Analysis, Calibration Procedure, and Ice Water Content Determination, *Am. Meteorol. Soc.*, 463–475, 390 doi:10.1175/JTECH1975.1, 2007b.
- DeMott, P. J., Cziczko D. J., Prenni A. J., Murphy D. M., Kreidenweis S. M., Thomson D. S., Borys R., and Rogers D. C.: Measurements of the concentration and composition of nuclei for cirrus formation, *PNAS*, 100 (25), 14655-14660, doi:10.1073/pnas.2532677100, 2003.
- 395 DeMott, P. J., Prenni, A. J., Liu, X., Kreidenweis, S. M., Petters, M. D., Twohy, C. H., ... Rogers, D. C. Predicting global atmospheric ice nuclei distributions and their impacts on climate. *Proceedings of the National Academy of Sciences*, 107(25), 11217–11222. <https://doi.org/10.1073/pnas.0910818107>, 2010.
- Formlabs: 3D Printing with Desktop Stereolithography: An Introduction for Professional Users. [online] Available from: <http://formlabs.com/media/upload/Intro-sla-whitepaper-04.pdf>, 2015.
- 400 Friedman, B., Ardon-Dryer, K., Carrasquillo, A., Daumit, K., Boulanger, K., Cross, E., Browne, E., Kroll, J., Thornton, J. and Cziczko, D.: CCN closure and composition analysis of droplet-forming aerosol, *AIP Conf. Proc.*, 1527, 832–835, doi:10.1063/1.4803400, 2013.
- Friedman, B., Zelenyuk, A., Beranek, J., Kulkarni, G., Pekour, M., Gannet Hallar, A., McCubbin, I.B., Thornton, J.A., and Cziczko, D. J. (2013). Aerosol measurements at a high-elevation site: Composition, size, and cloud condensation nuclei activity. *Atmospheric Chemistry and Physics*, 13(23), 11839–11851. <https://doi.org/10.5194/acp-13-11839-2013>
- 405 Hagiwara, T.: Current Status and Future Prospects of Laser Stereolithography, *Proc SPIE*, 5662, 644–648, doi:10.1117/12.596757, 2004.
- Hallar, A. G., Lowenthal, D. H., Chirokova, G., Borys, R. D., & Wiedinmyer, C.: Persistent daily new particle formation at a mountain-top location. *Atmospheric Environment*, 45(24), 4111–4115. 410 <https://doi.org/10.1016/j.atmosenv.2011.04.044>, 2011.



- Hallar, A. G., Petersen, R., McCubbin, I. B., Lowenthal, D., Lee, S., Andrews, E., & Yu, F. (2016). Climatology of New Particle Formation and Corresponding Precursors at Storm Peak Laboratory. *Aerosol and Air Quality Research*, 16(3), 816–826 <https://doi.org/10.4209/aaqr.2015.05.0341>.
- 415 Hiranuma, N., Möhler, O., Kulkarni, G., Schnaiter, M., Vogt, S., Vochezer, P., Järvinen, E., Wagner, R., Bell, D. M., Wilson, J., Zelenyuk, A., Cziczo, D. J., Jarvinen, E., Wagner, R., Bell, D. M., Wilson, J., Zelenyuk, A. and Cziczo, D. J.: Development and characterization of an ice-selecting pumped counterflow virtual impactor (IS-PCVI) to study ice crystal residuals, *Atmos. Meas. Tech.*, 9(April), 3817–3836, doi:10.5194/amt-9-3817-2016, 2016a.
- 420 Hiranuma, N., Möhler, O., Kulkarni, G., Schnaiter, M., Vogt, S., Vochezer, P., Jarvinen, E., Wagner, R., Bell, D. M., Wilson, J., Zelenyuk, A. and Cziczo, D. J.: Development and characterization of an ice-selecting pumped counterflow virtual impactor (IS-PCVI) to study ice crystal residuals, *Atmos. Meas. Tech.*, 9, 3817–3836, doi:10.5194/amt-9-3817-2016, 2016b.
- Hirst, E., Kaye, P. H., Greenaway, R. S., Field, P. and Johnson, D. W.: Discrimination of micrometre-sized ice and super-cooled droplets in mixed-phase cloud, *Atmos. Environ.*, 35, 33–47, 2001.
- 425 Jacobs, P. F.: *Rapid Prototyping & Manufacturing: Fundamentals of StereoLithography*, 1st ed., Society of Manufacturing Engineers, Dearborn., 1992.
- Kamphus, M., Etter-Mahl, M., Klimach, T., Drewnick, F., Keller, L., Cziczo, D. J., Mertes, S., Borrmann, S. and Curtius, J.: Chemical composition of ambient aerosol , ice residues and cloud droplet residues in mixed-phase clouds : single particle analysis during the Cloud and Aerosol Characterization Experiment, *Atmos. Chem. Phys.*, 10, 8077–8095, doi:10.5194/acp-10-8077-2010, 2010.
- 430 Kleinman, L. I., Daum, P. H., Lee, Y. N., Lewis, E. R., Sedlacek, A. J., Senum, G. I., Springston, S. R., Wang, J., Hubbe, J., Jayne, J., Min, Q., Yum, S. S. and Allen, G.: Aerosol concentration and size distribution measured below, in, and above cloud from the DOE G-1 during VOCALS-REx, *Atmos. Chem. Phys.*, 12(1), 207–223, doi:10.5194/acp-12-207-2012, 2012.
- 435 Koolik, L. P.: *Characterization of a 3D Printed Pumped Counterflow Virtual Impactor and an Aerodynamic Lens Concentrator*, Massachusetts Institute of Technology., 2017.
- Koop, T., Luo, B., Athanasios, T., and Peter, T.: Water activity as the determinant for homogeneous ice nucleation in aqueous solutions, *Nature*, 406, doi:10.1038/35020537, 2000.
- Korolev, A.: Limitations of the Wegener–Bergeron–Findeisen Mechanism in the Evolution of Mixed-Phase Clouds, *J. Atmos. Sci.*, 64, 3372–3375, doi:10.1175/JAS4035.1, 2007.
- 440 Korolev, A. V, Isaac, G. A., Cober, S. G., Strapp, J. W. and Hallett, J.: Microphysical characterization of mixed-phase clouds, *Q. J. R. Meteorol. Soc.*, 129, 39–65, doi:10.1256/qj.01.204, 2003.
- Korolev, A. V., Strapp, J. W., Isaac, G. A. and Nevzorov, A. N.: *The Nevzorov Airborne Hot-Wire LWC – TWC Probe : Principle of Operation and Performance Characteristics*, *Am. Meteorol. Soc.*, 1495–1510, 1998.
- Kulkarni, G., Pekour, M., Afchine, A., Murphy, D. M. and Cziczo, D. J.: Comparison of Experimental and Numerical Studies



- 445 of the Performance Characteristics of a Pumped Counterflow Virtual Impactor, *Aerosol Sci. Technol.*, 45(3), 382–392, doi:10.1080/02786826.2010.539291, 2011.
- Kupiszewski, P., Weingartner, E., Vochezer, P., Schnaiter, M., Bigi, A., Gysel, M., Rosati, B., Toprak, E., Mertes, S. and Baltensperger, U.: The Ice Selective Inlet: A novel technique for exclusive extraction of pristine ice crystals in mixed-phase clouds, *Atmos. Meas. Tech.*, 8(8), 3087–3106, doi:10.5194/amt-8-3087-2015, 2015.
- 450 Larson, B. H. and Swanson, B. D.: Experimental investigation of the homogeneous freezing of aqueous ammonium sulfate droplets, *J. Phys. Chem. A*, 110(5), 1907–1916, doi:10.1021/jp0542701, 2006.
- Li, L., & Pomeroy, J. W. (1997). Probability of occurrence of blowing snow. *Journal of Geophysical Research: Atmospheres*, 102(D18), 21955–21964.
- 455 Lohmann, U. and Hoose, C.: Sensitivity studies of different aerosol indirect effects in mixed-phase clouds, *Atmos. Chem. Phys.*, 9, 8917–8934, 2009.
- Lohmann, U., Lüönd, F., & Mahrt, F. (2016). *An introduction to clouds: From the microscale to climate*. Cambridge University Press.
- Lowenthal, D. H., Hallar, A. G., David, R. O., McCubbin, I. B., Borys, R. D., & Mace, G. G. (2019). Mixed-phase
- 460 orographic cloud microphysics during StormVEx and IFRACS. *Atmospheric Chemistry and Physics*, 19(8), 5387–5401. <https://doi.org/10.5194/acp-19-5387-2019>
- Mertes, S., Verheggen, B., Walter, S., Connolly, P. J., Ebert, M., Schneider, J., Bower, K. N., Cozic, J., Weinbruch, S., Baltensperger, U. and Weingartner, E.: Counterflow Virtual Impactor Based Collection of Small Ice Particles in Mixed-Phase Clouds for the Physico-Chemical Characterization of Tropospheric Ice Nuclei: Sampler Description and First Case
- 465 Study, *Aerosol Sci. Technol.*, 41(9), 848–864, doi:10.1080/02786820701501881, 2007.
- Murray, G. L. D., Kimball, K. D., Hill, L. B., Hislop, J. E. and Weathers, K. C.: Long-Term Trends in Cloud and Rain Chemistry on Mount Washington, New Hampshire, *Water Air Soil Pollut.*, 224(1653), 1–14, doi:10.1007/s11270-013-1653-7, 2013.
- Patade, S., Shete, S., Malap, N., Kulkarni, G. and Prabha, T. V: Observational and simulated cloud microphysical features of
- 470 rain formation in the mixed phase clouds observed during CAIPEEX, *Atmos. Res.*, 169, 32–45, doi:10.1016/j.atmosres.2015.09.018, 2015.
- Pekour, M. S. and Cziczo, D. J.: Wake Capture, Particle Breakup, and Other Artifacts Associated with Counterflow Virtual Impaction, *Aerosol Sci. Technol.*, 45(6), 758–764, doi:10.1080/02786826.2011.558942, 2011.
- Pruppacher, H. R. and Klett, J. D.: *Microphysics of Clouds and Precipitation*, 2nd ed., Kluwer Academic Publishers, Dordrecht., 1997.
- 475 Roesch, M. and Cziczo, D.J.: Wet particle generation with a 3D printed nebulizer, in preparation.
- Roesch, M., Roesch, C. and Cziczo, D. J.: Dry particle generation with a 3-D printed fluidized bed generator, *Atmos. Meas. Tech.*, 10, 1999–2007, 2017.



- Rogers, R. R. and Yau, M. K.: A Short Course in Cloud Physics, 3rd ed., Elsevier Science, Tarrytown., 1989.
- 480 Seidel, T. M., Grant, A. N., Pszenny, A. A. P. and Allman, D. J.: Dewpoint and Humidity Measurements and Trends at the Summit of Mount Washington, New Hampshire, 1935 – 2004, *Am. Meteorol. Soc.*, 20, 5629–5641, doi:10.1175/2007JCLI1604.1, 2007.
- Seidel, T. M., Weihrauch, D. M., Kimball, K. D., Pszenny, A. A. P., Soboleski, R., Crete, E. and Murray, G.: Evidence of Climate Change Declines with Elevation Based on Temperature and Snow Records from 1930s to 2006 on Mount
485 Washington, New Hampshire, Arctic, Antarct. Alp. Res., 41(3), 362–372, doi:10.1657/1938-4246-41.3.362, 2009.
- Shupe, M., Daniel, J. S., De Boer, G., Eloranta, E. W., Kollias, P., Long, C. N., Luke, E. P., Turner, D. D. and Verlinde, J.: A Focus on Mixed-Phase Clouds, *Am. Meteorol. Soc.*, 1549–1562, doi:10.1175/2008BAMS2378.1, 2008.
- Shupe, M. D., Matrosov, S. Y. and Uttal, T.: Arctic Mixed-Phase Cloud Properties Derived from Surface-Based Sensors at SHEBA, *Am. Meteorol. Soc.*, 697–711, 2006.
- 490 Slowik, J. G., Cziczko, D. J. and Abbatt, J. P. D.: Analysis of cloud condensation nuclei composition and growth kinetics using a pumped counterflow virtual impactor and aerosol mass spectrometer, *Atmos. Meas. Tech.*, 4(8), 1677–1688, doi:10.5194/amt-4-1677-2011, 2011.
- Smith, A. A.: The Mount Washington Observatory - 50 Years Old, *Bull. Am. Meteorological Soc.*, 63(9), 986–995, 1982.
- Storelvmo, T., Kristjansson, J. E. and Lohmann, U.: Aerosol Influence on Mixed-Phase Clouds in CAM-Oslo, *J. Atmos. Sci.*,
495 65, 3214–3230, doi:10.1175/2008JAS2430.1, 2008.
- Strapp, J. W., Lilie, L. E., Ratvasky, T. P., Davison, C. and Dumont, C.: Isokinetic TWC Evaporator Probe: Development of the IKP2 and Performance Testing for the HAIC-HIWC Darwin 2014 and Cayenne-2015 Field Campaigns, *Am. Inst. Aeronaut. Astronaut.*, (June), 1–28, doi:10.2514/6.2016-4059, 2016.
- Tsushima, Y., Emori, S., Ogura, T., Kimoto, M., Webb, M. J., Williams, K. D., Ringer, M. A., Soden, B. J., Li, B. and
500 Andronova, N.: Importance of the mixed-phase cloud distribution in the control climate for assessing the response of clouds to carbon dioxide increase: a multi-model study, *Clim. Dyn.*, doi:10.1007/s00382-006-0127-7, 2006.
- Verheggen, B., Cozic, J., Weingartner, E., Bower, K., Mertes, S., Connolly, P., Gallagher, M., Flynn, M., Choulaton, T. and Baltensperger, U.: Aerosol partitioning between the interstitial and the condensed phase in mixed-phase clouds, *J. Geophys. Res.*, 112(1), 1–13, doi:10.1029/2007JD008714, 2007.
- 505 Verlinde, J., Harrington, J. Y., McFarquhar, G. M., Yannuzzi, V. T., Avramov, A., Greenberg, S., Johnson, N., Zhang, G., Poellot, M. R., Mather, J. H., Turner, E., Eloranta, E. W., Zak, B. D., Prenni, A. J., Daniel, J. S., Kok, G. L., Tobin, D. C., Holz, R., Sassen, K., Spangenberg, D., Minnis, P., Tooman, T. P., Ivey, M. D., Richardson, S. J., Bahrman, C. P., Shupe, M., DeMott, P. J., Heymsfield, A. J. and Schofield, R.: The mixed-phase arctic cloud experiment, *Am. Meteorol. Soc.*, (July 2006), 205–221, doi:10.1175/BAMS-88-2-205, 2007.
- 510 Wang, B., Lambe, A. T., Massoli, P., Onasch, T. B., Davidovits, P., Worsnop, D. R. and Knopf, D. A.: The deposition ice nucleation and immersion freezing potential of amorphous secondary organic aerosol: Pathways for ice and mixed-phase cloud formation, *J. Geophys. Res.*, 117, 1–12, doi:10.1029/2012JD018063, 2012.



Wong, K. V and Hernandez, A.: A Review of Additive Manufacturing, ISRN Mech. Eng., 2012, doi:10.5402/2012/208760, 2012.

515 **Tables**

Table 1: SPIDER Flows

Component	L-PCVI			Chamber	PCVI		
	PF	AF	SF		PF	AF	SF
Flow (SL min ⁻¹)	43.0	10.0	6.7	6.7	7.7	2.0	1.0

520

Table 2: L-PCVI Flow Tests

525

AF-to-IF Ratio	Flows (L min ⁻¹)			
	AF	IF	PF	SF
0.14*	7.0	50.0	51.0	6.5
0.16	12.0	72.0	78.0	6.5
0.23	12.0	50.0	56.0	6.5

*Refers to the ratio and flows used by Hiranuma et al. (2016).



Figures

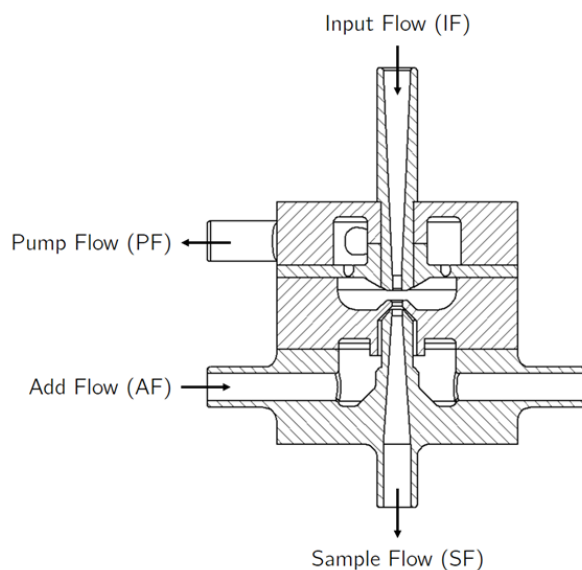


Figure 1: Cross-sectional view of the 3D printed SPIDER PCVI with flows labelled. The 3D printed PCVI features the improved slanted input nozzle suggested by Kulkarni et al. (2011); otherwise, the design is the same as considered by Kulkarni et al. (2011).

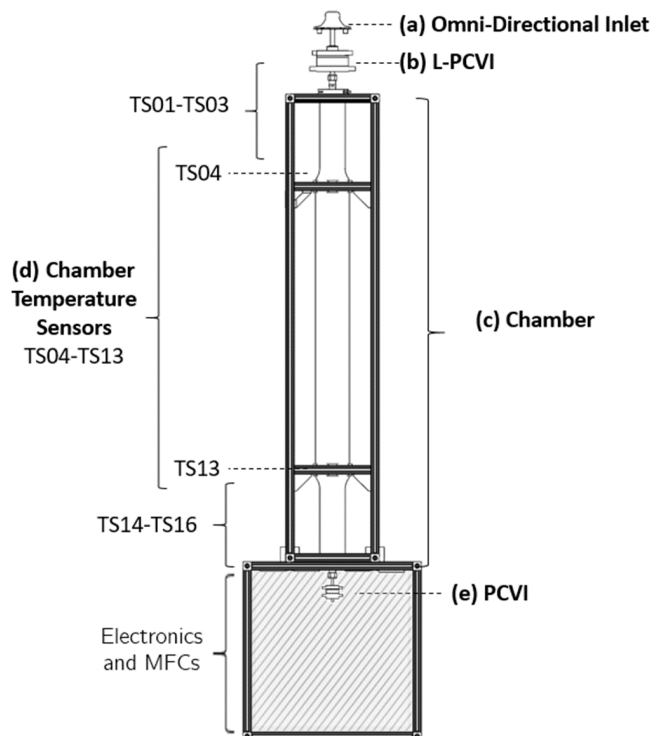


Figure 2: Schematic of SPIDER with its components labelled. (a) The omni-directional inlet prevents large rain hydrometeors from entering SPIDER. (b) The L-PCVI (Hiranuma et al., 2016) separates interstitial aerosol from the droplets and ice crystals. (c) The chamber is cooled and held at ice saturation to evaporate droplets. (d) Thermocouples report the temperature in the chamber. (e) The PCVI downstream separates evaporated droplet residuals from ice crystals.

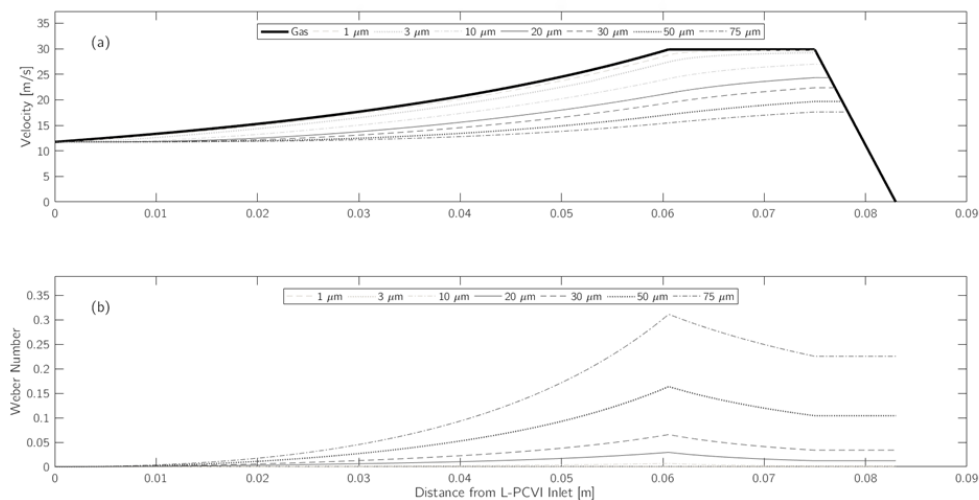


Figure 3: (a) Velocity calculated for droplet sizes and gas shown as a function of distance from the L-PCVI inlet. (b) The corresponding Weber number calculated along the L-PCVI inlet.

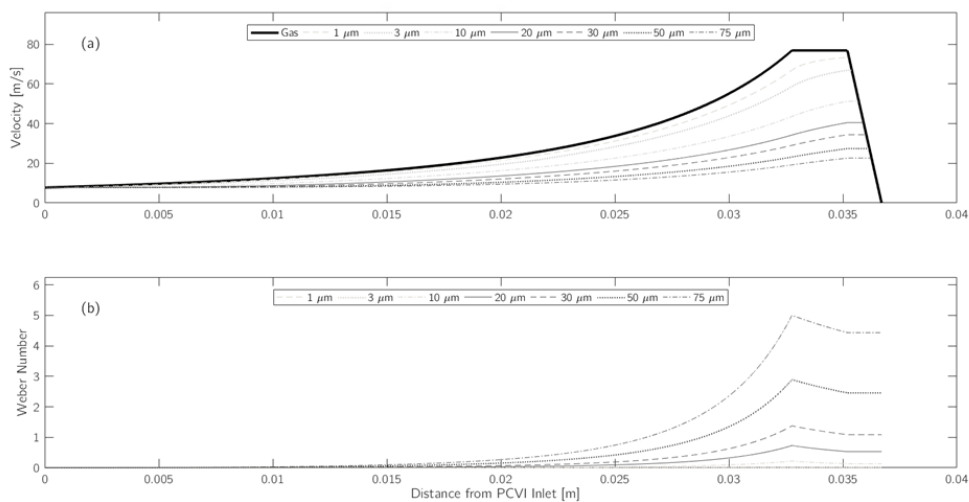


Figure 4: (a) Velocity calculated for droplet sizes and gas shown as a function of distance from the PCVI inlet. (b) The corresponding Weber number calculated along the PCVI inlet.

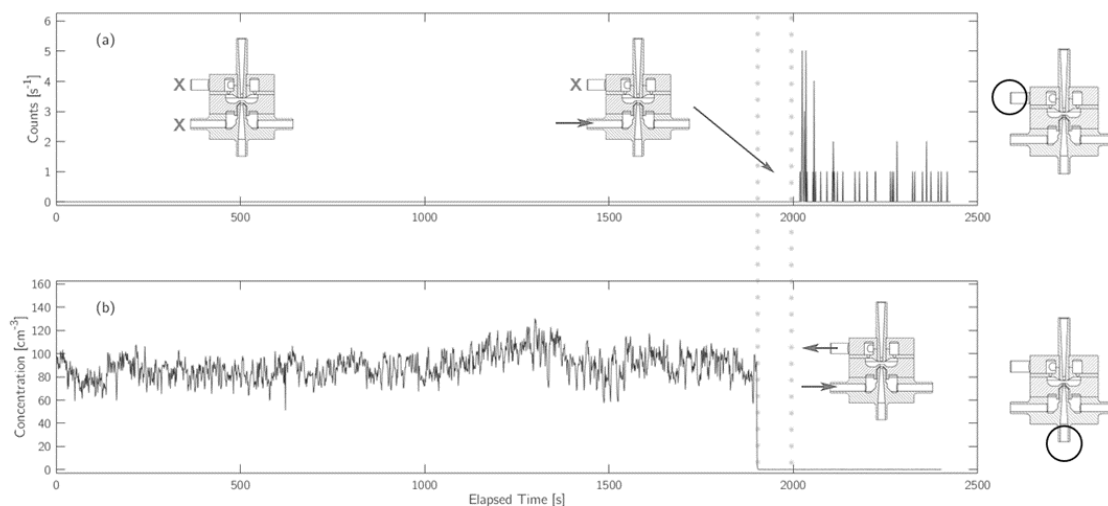


Figure 5: Concurrent time series of particles detected in the (a) PF and the (b) SF of the L-PCVI. The flows into the PF and AF were turned on between 1,700-1,900 s. Note that particles were detected only in the SF until the flows were turned on, at which point the particles are counted in the PF.

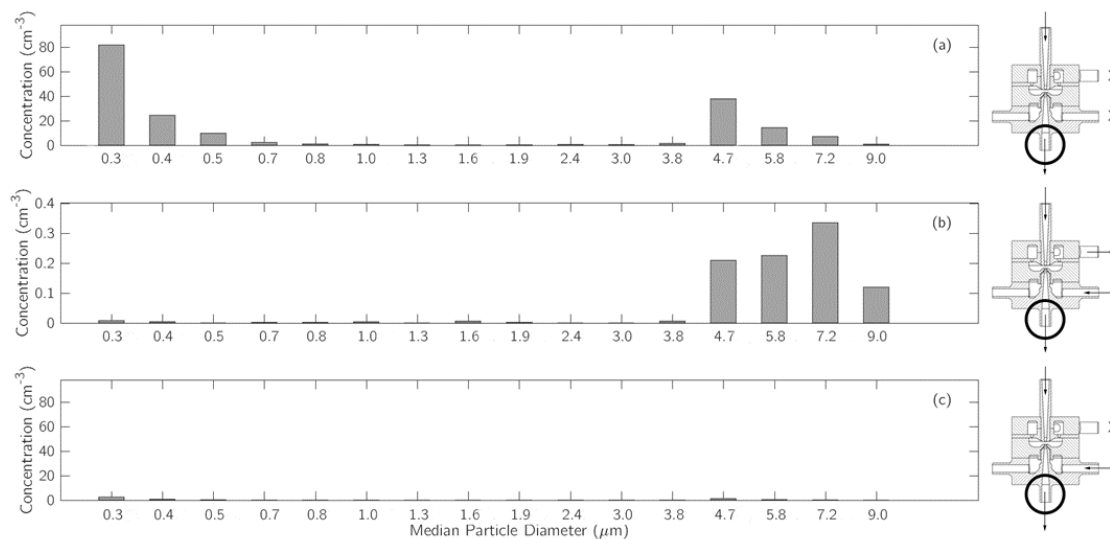


Figure 6: Droplet transmission through the L-PCVI under varying flow scenarios. The average number concentration of particles out of the SF of the L-PCVI is plotted against median particle diameter for (a) AF and PF off, (b) AF and PF on, and (c) only AF on.

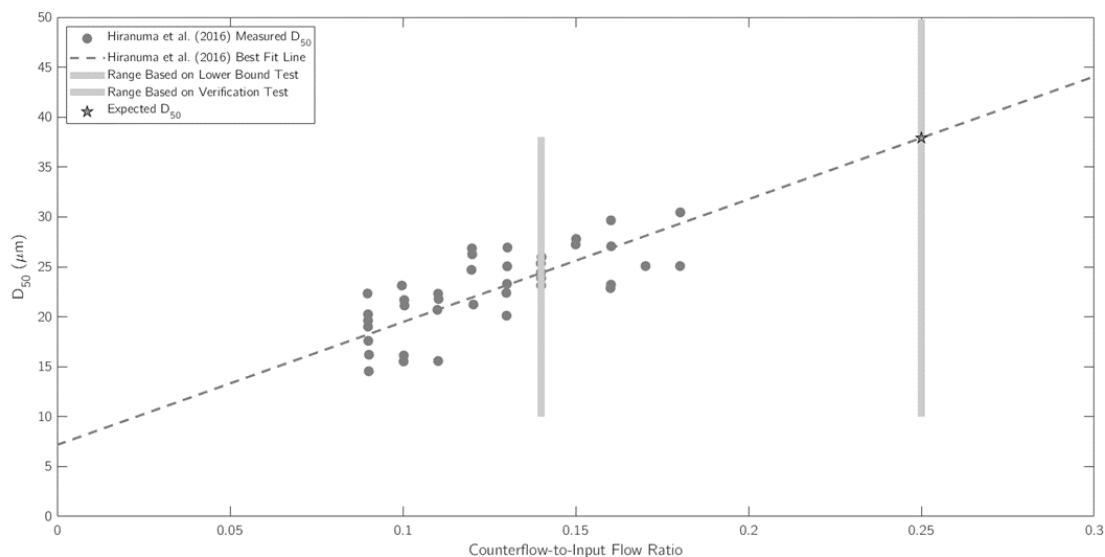


Figure 7: D50 as a function of counterflow to input flow ratio from this work and Hiranuma et al. (2016). The grey dashed line and points refer to the values from Hiranuma et al. (2016). The vertical lines indicate the ranges from the lower bound test (light grey) and verification test (dark grey). The star is the anticipated D50 using SPIDER’s flow ratio and the Hiranuma et al. (2016) data fit line.

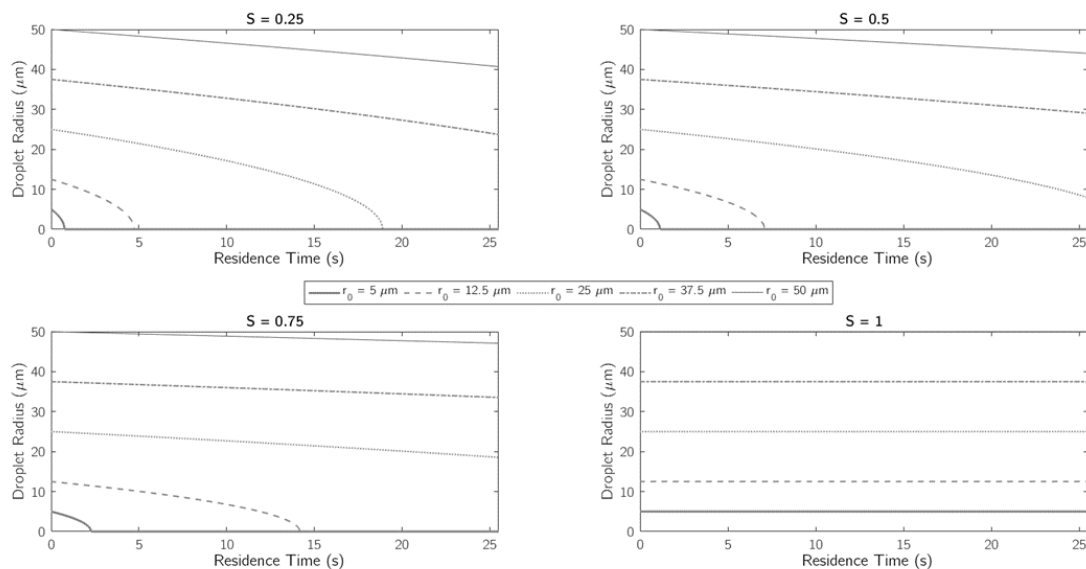


Figure 8: Droplet size, as a function of time (i.e., evaporation time) for five initial droplet sizes relevant to SPIDER for saturation ratios of (a) 0.25, (b) 0.5, (c) 0.75, and (d) 1.0.

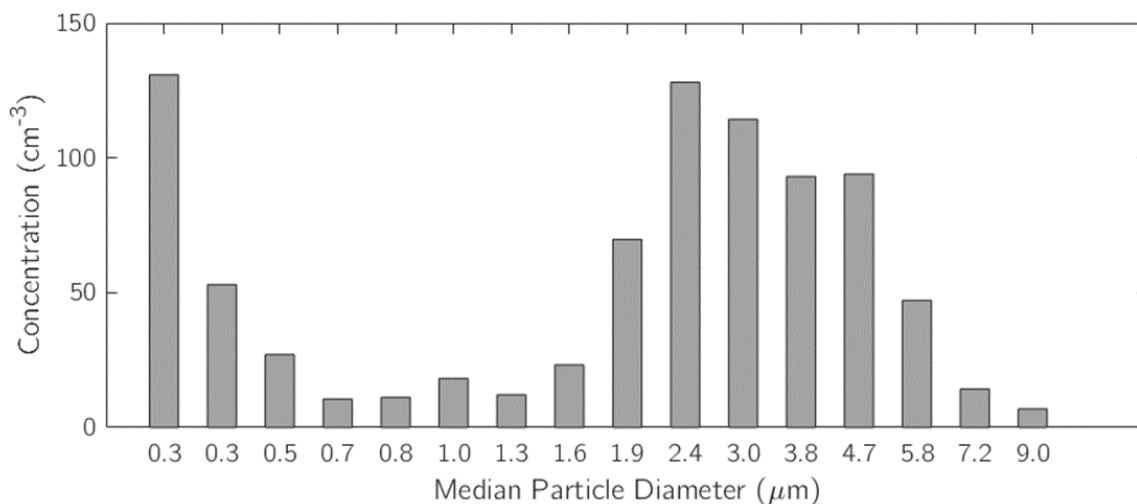


Figure 9: Number concentration as a function of particle diameter for ice crystals travelling through the chamber. Ambient air was introduced to the cooled chamber with the PCVI on. Droplets were introduced into the cooled chamber with the PCVI on. The results shown are the difference between these two averages, reflecting the size distribution from ice crystals alone.

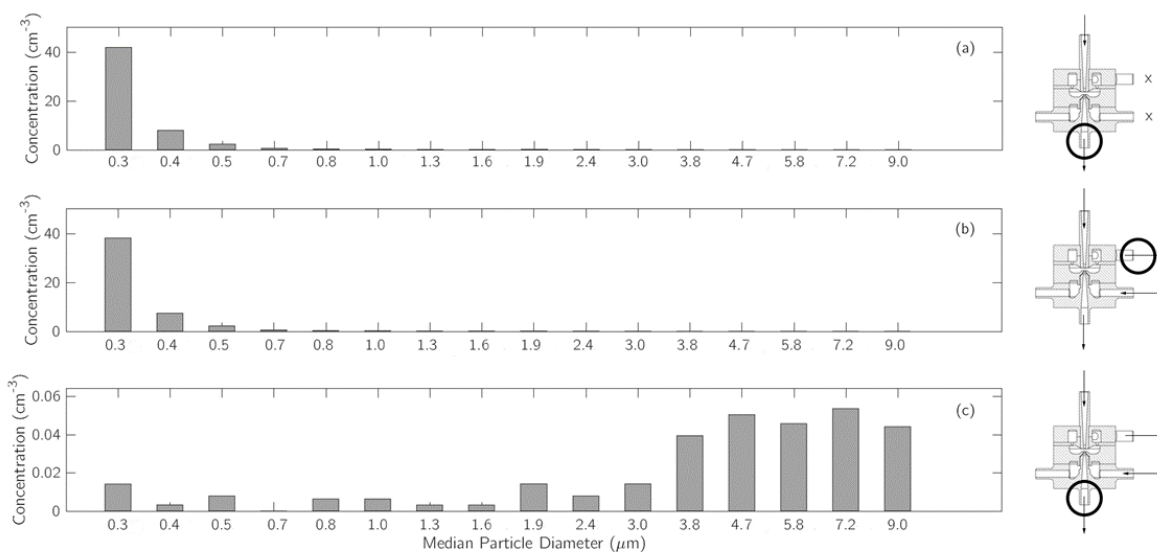


Figure 10: Number concentration as a function of particle diameter for three PCVI verification tests. (a) A control experiment with the PCVI is turned off with the OPS in the SF. (b) The aerosol concentration for sizes below the PCVI cutpoint with the PCVI turned on with the OPS in the PF. (c) The PCVI is turned on with the OPS in the SF.

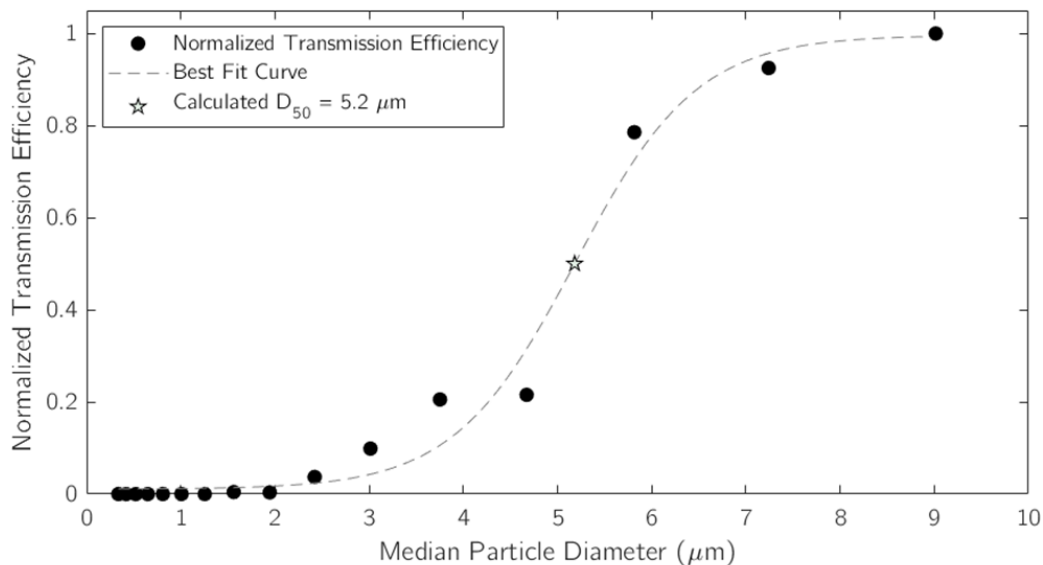


Figure 11: Transmission efficiency as a function of particle diameter (solid circles) fit with a sigmoidal curve (dashed line). The star represents the size at which 50% of particles are transmitted (the experimental D50).

540

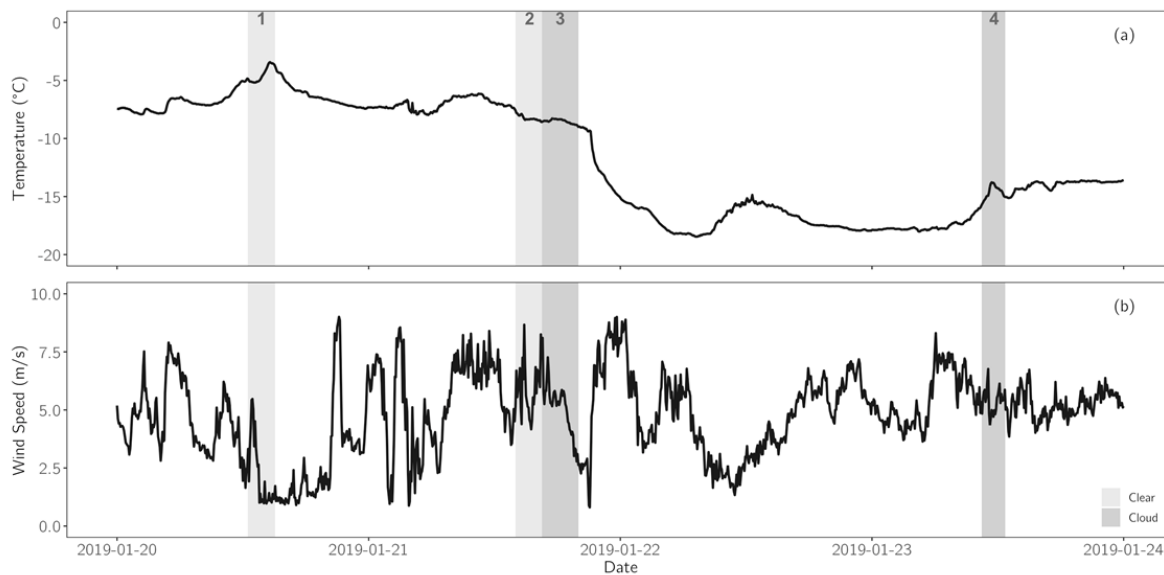


Figure 12: Meteorological conditions during sampling periods at SPL. Temperature (a); Wind Speed (b); Light gray areas represent clear conditions, dark gray areas represent cloudy conditions.

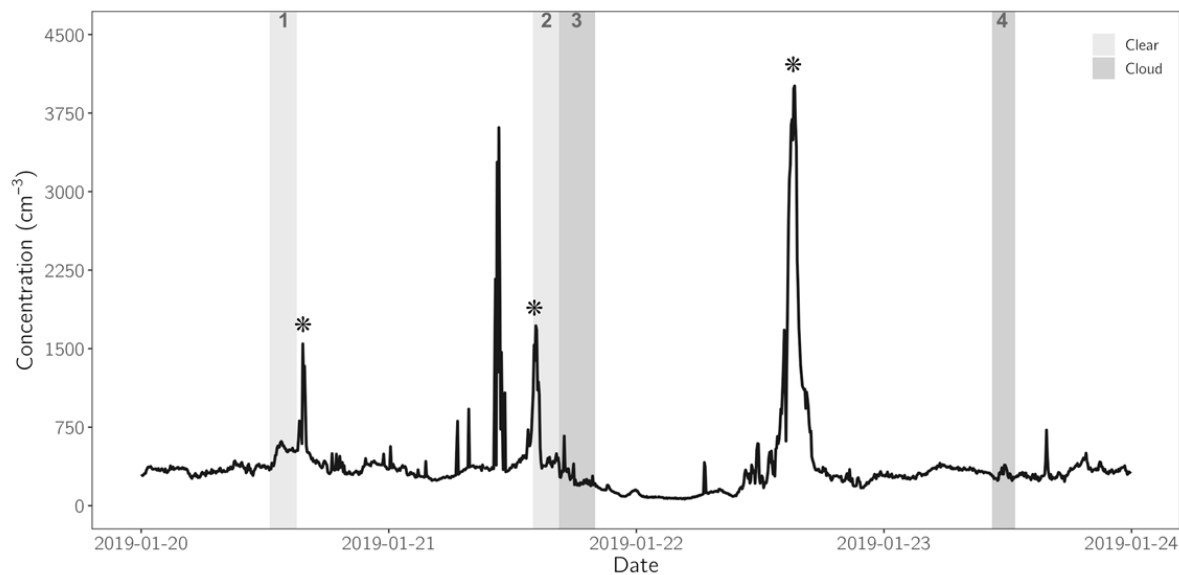


Figure 13: SMPS background concentration at SPL during the study period. Light gray areas represent clear conditions, dark gray areas represent cloudy conditions. Asterisks denote possible new particle formation. Other spikes are most likely caused by snow machinery.

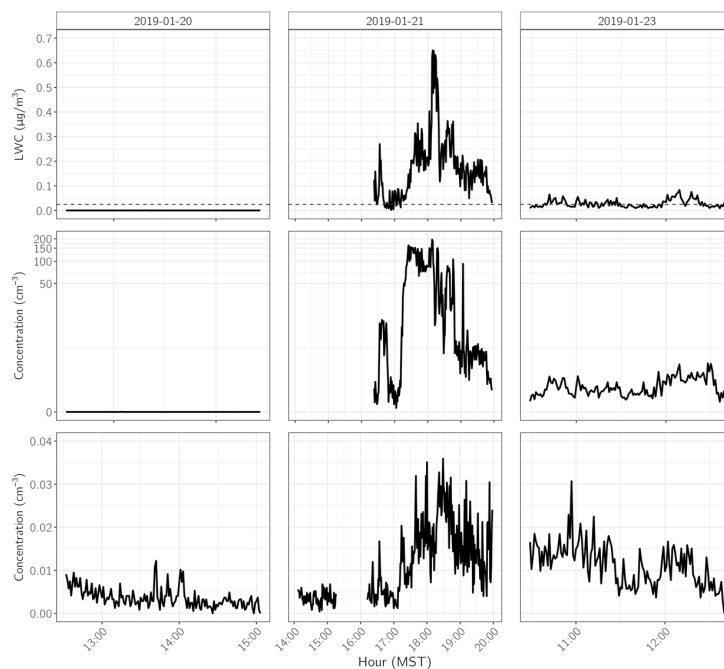


Figure 14: Schematic of SPIDER with its components labelled. (a) The omni-directional inlet prevents large rain hydrometeors from entering SPIDER. (b) The L-PCVI (Hiranuma et al., 2016) separates interstitial aerosol from the droplets and ice crystals. (c) The chamber is cooled and held at ice saturation to evaporate droplets. (d) Thermocouples report the temperature in the chamber. (e) The PCVI downstream separates evaporated droplet residuals from ice crystals.

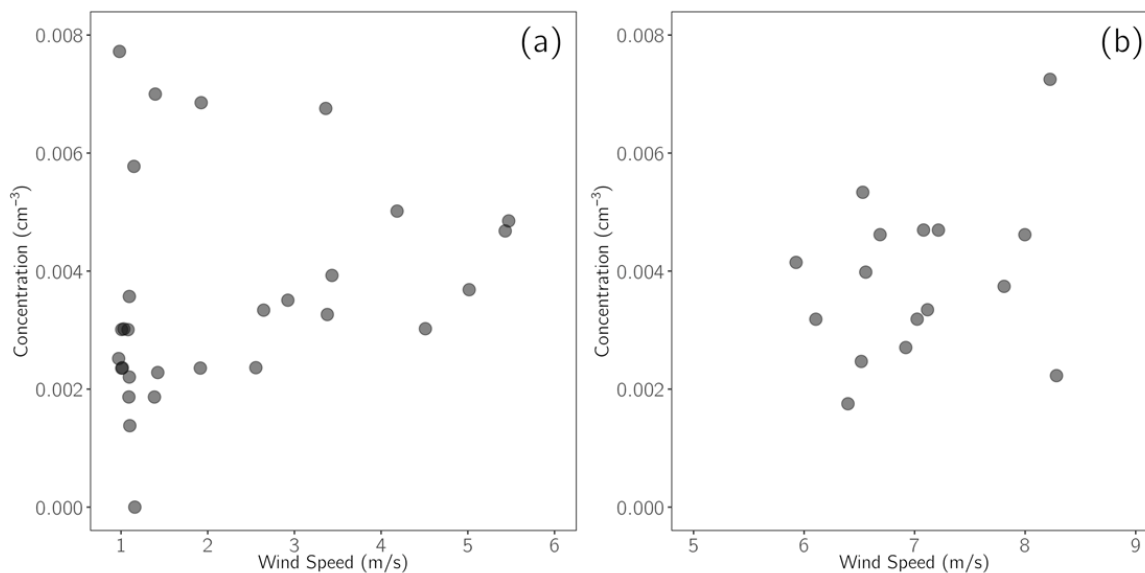


Figure 15: Ice crystal residual particle concentration as a function of wind speed during clear periods: period 1, 1/20/2019 (a); period 2, 1/21/2019 (b).

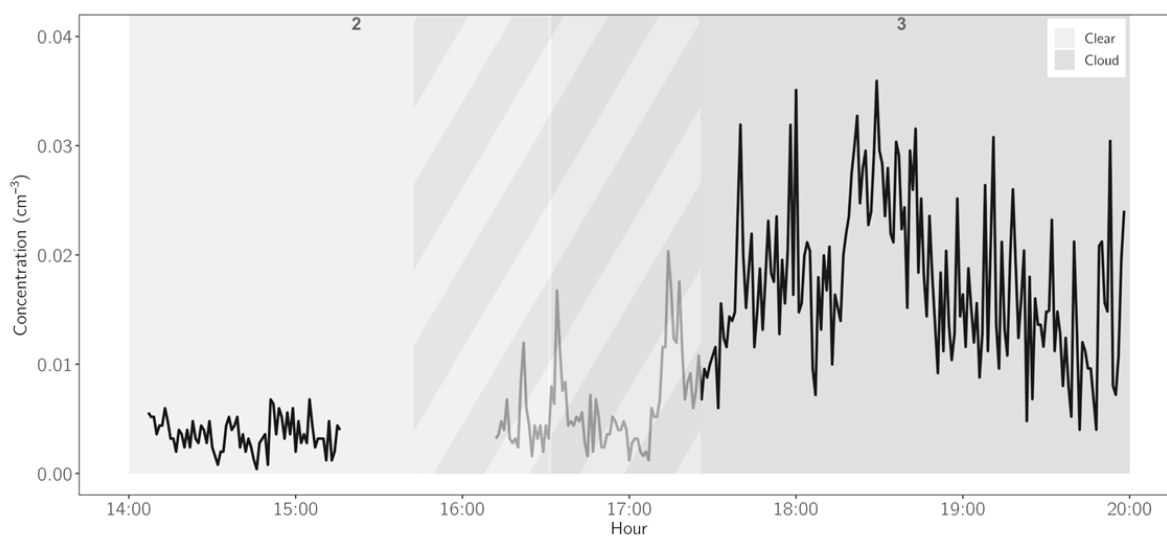


Figure 16: Ice crystal residual concentrations of the SP2-XR from clear (light gray) to cloudy (dark gray) conditions. The transition period is depicted in striped shading.

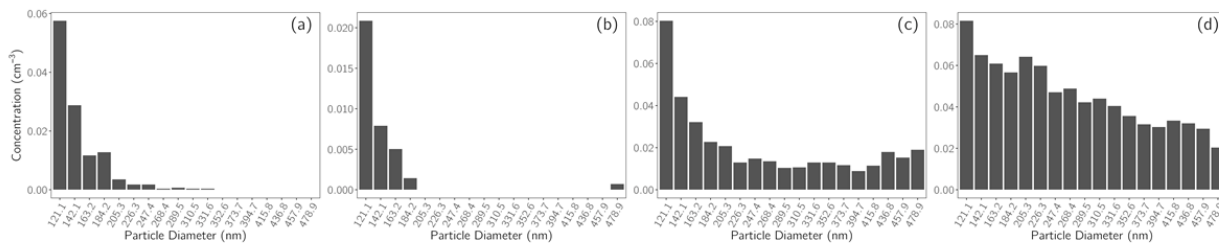


Figure 17: SP2-XR average ice crystal residual concentration. Clear conditions during periods 1 and 2 (a, b) and cloudy conditions during periods 3 and 4 (c, d), respectively.